NANO · MICRO small
www.small-journal.com

NiSe and CoSe Topological Nodal-Line Semimetals: A Sustainable Platform for Efficient Thermoplasmonics and Solar-Driven Photothermal Membrane Distillation

Shir Abramovich, Debasis Dutta, Carlo Rizza, Sergio Santoro, Marco Aquino, Anna Cupolillo, Jessica Occhiuzzi, Mauro Francesco La Russa, Barun Ghosh, Daniel Farias, Andrea Locatelli, Danil W. Boukhvalov, Amit Agarwal, Efrem Curcio, Maya Bar Sadan,* and Antonio Politano**

The control of heat at the nanoscale via the excitation of localized surface plasmons in nanoparticles (NPs) irradiated with light holds great potential in several fields (cancer therapy, catalysis, desalination). To date, most thermoplasmonic applications are based on Ag and Au NPs, whose cost of raw materials inevitably limits the scalability for industrial applications requiring large amounts of photothermal NPs, as in the case of desalination plants. On the other hand, alternative nanomaterials proposed so far exhibit severe restrictions associated with the insufficient photothermal efficacy in the visible, the poor chemical stability, and the challenging scalability. Here, it is demonstrated the outstanding potential of NiSe and CoSe topological nodal-line semimetals for thermoplasmonics. The anisotropic dielectric properties of NiSe and CoSe activate additional plasmonic resonances. Specifically, NiSe and CoSe NPs support multiple localized surface plasmons in the optical range, resulting in a broadband matching with sunlight radiation spectrum. Finally, it is validated the proposed NiSe and CoSe-based thermoplasmonic platform by implementing solar-driven membrane distillation by adopting NiSe and CoSe nanofillers embedded in a polymeric membrane for seawater desalination. Remarkably, replacing Ag with NiSe and CoSe for solar membrane distillation increases the transmembrane flux by 330% and 690%, respectively. Correspondingly, costs of raw materials are also reduced by 24 and 11 times, respectively. The results pave the way for the advent of NiSe and CoSe for efficient and sustainable thermoplasmonics and related applications exploiting sunlight within the paradigm of the circular blue economy.

In recent years, the opportunity to exploit metal nanostructures as nanosources of heat, tunable with light, has originated the fast-growing field of thermoplasmonics.[1] Upon illumination at the plasmon frequency, metal NPs display enhanced light absorption, enabling efficient light-to-heat conversion.[1a] Recently, thermoplasmonic effects have been successfully exploited mainly for biomedical applications, such as photothermal cancer therapy,[2] neural stimulation,[3] bacteria killing,[4] intracellular delivery of miRNA,[5] photothermal biosensors for SARS-CoV-2 detection.[6] Additionally, thermoplasmonic effects also play a pivotal role in photothermal actuators,[7] nanofurnaces for heterogeneous catalysis,[8] and solar-driven water evaporation.[9] In particular, thermoplasmonics could provide a relevant contribution for addressing the global water shortage, which represents one of the most vital open challenges for mankind,[10] further exacerbated by climate change[11] and particularly relevant in developing countries.[12] Concomitantly, the urgent need for a green transition[13] has boosted the advent of sustainable

S. Abramovich, M. Bar Sadan
Department of Chemistry
Ben-Gurion University
Be'er Sheva 8410501, Israel
E-mail: barsadan@bgu.ac.il

The ORCID identification number(s) for the author(s) of this article can be found under https://doi.org/10.1002/smll.202201473.

© 2022 The Authors. Small published by Wiley-VCH GmbH. This is an open access article under the terms of the Creative Commons Attribution-NonCommercial License, which permits use, distribution and reproduction in any medium, provided the original work is properly cited and is not used for commercial purposes.

DOI: 10.1002/smll.202201473

D. Dutta, B. Ghosh, A. Agarwal
Department of Physics
Indian Institute of Technology Kanpur
Kanpur 208016, India

C. Rizza, J. Occhiuzzi, A. Politano
Department of Physical and Chemical Sciences
University of L'Aquila
L'Aquila 67100, Italy
E-mail: antonio.politano@univaq.it

S. Santoro, M. Aquino, E. Curcio
Department of Environmental Engineering
University of Calabria
Via Pietro Bucci CUBO 44A, Rende, CS 87036, Italy
E-mail: efrem.curcio@unical.it

technologies for seawater desalination,[14] enabling the integration of renewable energy sources, such as solar power, in desalination processes,[15] today dominated by membranes.[16] Among the various membrane technologies, membrane distillation (MD) affords a reliable prospect to recover simultaneously fresh water from seawater and brine at competitive costs.[17] Explicitly, MD is based on the evaporation and diffusion of water through a microporous hydrophobic membrane under a vapor pressure gradient.[10c,18] Although unlimited by osmotic and concentration polarization phenomena affecting pressure-driven operations, such as reverse osmosis,[19] the efficiency of MD is severely reduced (even by 30–50%[20]) by temperature polarization,[20] which consists in the reduction of the temperature at the feed side, within the boundary layer adjacent to the membrane interface, as a result of the removal of the latent heat of vaporization associated to the transmembrane flux of water vapor.

While MD unquestionably still faces critical technological challenges, the use of radically innovative physicochemical concepts and processes, enabled by novel materials, could provide step-change improvements. In this respect, the localized heating at the water vapor–liquid interface achieved by light-to-heat conversion in photothermal materials has recently opened unprecedented opportunities in MD.[21] Using photothermal materials in MD could be crucial to implementing an environment-friendly green technology, exploiting renewable energy sources, such as solar power, to achieve efficient solar desalination.[15] In particular, photothermal MD implemented with plasmonic Ag nanofillers in hydrophobic polymeric membranes was shown to increase the transmembrane flux by one order of magnitude when irradiated with UV light.[10c,22] Accordingly, thermoplasmonic effects, promoted under solar irradiation, could be exploited to implement an innovative photothermal MD unit powered by sunlight, enabling its installation in remote areas without electric power grids for producing potable water for isolated communities, only using solar power. However, the use of Ag implies i) high costs impeding industrial scale-up and ii) an inefficient matching with sunlight radiation spectrum.

In general, replacing Ag and Au with cheap materials, exhibiting plasmonic resonances matching with the solar spectrum is one of the main open challenges of the whole plasmonic community.[23] Recently, several candidates for have emerged, such as nitrides (TiN[24] and HfN[25]), SnS_2[26]/$SnSe_2$,[27] Xenes (phosphorene,[28] arsenene,[29] stanene[30]), titanium carbides (namely, MXenes[31]), metal oxides,[32] etc. However, most of them have poor photothermal efficacy[10e] and high chemical instability with spontaneous oxidation already at room temperature, as in the case of Xenes[33] or tin dichalcogenides.[34]

Historically, individual plasmonic materials were initially identified mainly by intuition, trial, and error, and analogy to other materials, often with successive theoretical models to unveil their connection with band structure.[35] However, the recent efforts to perform a systematic analysis of band structure[36] can provide step-change support in the quest of photothermal materials with desired features in terms of excitation spectrum and light-to-heat conversion efficiency.[35a] Such a materials genome approach, now implemented in open-source databases,[37] is ideal for achieving a band-structure engineered platform for thermoplasmonics and related applications. In particular, the crystal anisotropy,[38] with corresponding anisotropic optical properties, offers novel functionalities for applications in plasmonics.[39] As a matter of fact, electromagnetic anisotropy is commonly adopted in engineering several optical devices, such as polarizers,[40] wave plates,[41] hyper-lenses,[42] spatial optical filters,[43] and phase matching components.[44] In principle, electromagnetic anisotropy could open new excitation channels with superior photothermal efficiency by improving the matching with the sunlight radiation spectrum.

Here, we demonstrate that the anisotropic optical properties of NiSe and CoSe make them a suitable platform for solar-driven thermoplasmonics, by combining theoretical predictions based on their band structure and dielectric properties, up to a direct validation carried out by fabricating photothermal nanocomposite hydrophobic membranes with NiSe and CoSe nanofillers. Outstandingly, the replacement of Ag (widely recognized as a state-of-the-art reference for thermoplasmonics) with NiSe and CoSe nanoscale thermal hotspots enables a significantly improved efficiency of solar membrane distillation, with an increase of transmembrane flux by 330% and 690% and with a reduction of costs by 24 and 11 times, respectively.

Bulk NiSe and CoSe crystallize in the space group $P6_3/mmc$ (group no: 194) with a hexagonal closed packing (hcp) structure held by covalent bonds. The unit cell of NiSe (CoSe) contains two Ni (Co) and two Se atoms with a bond length of 2.50 Å (2.48 Å). Their crystal symmetries include three vertical mirror planes, three vertical glide mirror planes, and a horizontal

A. Cupolillo
Department of Physics
University of Calabria
Via P. Bucci cubo 31/C, Rende, CS 87036, Italy
M. F. L. Russa
Department of Biology, Ecology, and Earth Sciences
Università della Calabria
Via Pietro Bucci, cubo 12/B, Arcavacata di, Rende, CS 87036, Italy
D. Farias
Departamento de Física de la Materia Condensada
Universidad Autónoma de Madrid
Madrid 28049, Spain
D. Farias
Instituto "Nicolás Cabrera"
Campus de Cantoblanco
Madrid 28049, Spain
D. Farias
Condensed Matter Physics Center (IFIMAC)
Universidad Autónoma de Madrid
Madrid 28049, Spain
A. Locatelli
Elettra-Sincrotrone S.C.p.A
S.S. 14-km 163.5 in AREA Science Park, Trieste 34149, Italy
A. Locatelli
College of Science
Institute of Materials Physics and Chemistry
Nanjing Forestry University
Nanjing 210037, P. R. China
E. Curcio
Seligenda Membrane Technologies s.r.l.
c/o University of Calabria
Via P. Bucci Cubo 45A, Rende, CS 87036, Italy
D. W. Boukhvalov
Ilse Katz Institute for Nanoscale Science and Technology
Ben Gurion University
Be'er Sheva 8410501, Israel

© 2022 The Authors. Small published by Wiley-VCH GmbH

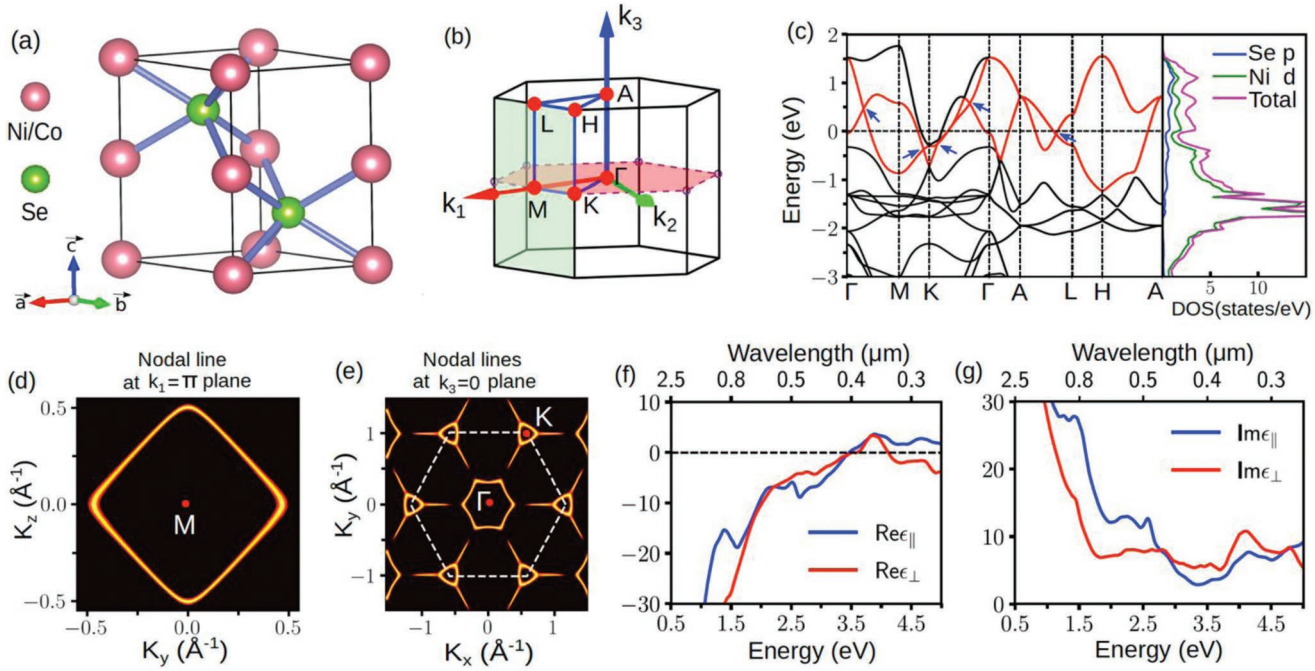

Figure 1. a) Crystal structure of bulk NiSe (CoSe). Green and red balls represent Se and Ni (Co) atoms, respectively. b) The hexagonal Brillouin zone of NiSe (CoSe) with different high symmetric points marked. Here, k_i with i = 1,2,3 denote the reciprocal lattice vectors. The $k_3 = 0$ and $k_1 = \pi$ mirror invariant planes are shaded in red and green, respectively. c) Electronic band structure and the DOS of NiSe. The red-colored bands denote the states originating multiple Dirac nodal lines (fourfold degenerate) in the mirror invariant momentum planes shown in panel b). The crossing points are indicated by blue arrows. The nodal line structure is represented in the d) $k_1 = \pi$ and e) the $k_3 = 0$ planes, respectively. The color scale expresses the local bandgap between the bands near the Fermi level, highlighted in red in panel (c). Yellow and black indicate zero and finite bandgap, respectively. Thus, the yellow curves in (d) and (e) represent the structure of the nodal lines in the *k*-space. Panels (e) and (f) report the real and imaginary parts of the in-plane ($\varepsilon_{\parallel}$) and out-of-plane ($\varepsilon_{\perp}$) components of the bulk dielectric function for NiSe, respectively.

mirror plane. Moreover, their structure hosts an inversion center and sixfold screw rotation symmetry along the vertical direction, which plays a significant role in protecting band crossing points in the electronic structure.

Near the Fermi level, the dominant orbital contributions arise from Ni (Co) *d* orbitals and Se *p* orbitals. In particular, *d* orbitals of Ni (Co) originate nearly flat-looking bands around ≈1.0 eV below the Fermi level (**Figure 1**c for NiSe; and Figure S1 in the Supporting Information, for CoSe), with corresponding peaks in the density of states (DOS). Such a large DOS around the Fermi level increases the probability of optical transitions. Interestingly, the two bands near the Fermi level (highlighted in red in Figure 1c) give rise to multiple Dirac nodal-line structures (fourfold degenerate) in different mirror invariant momentum planes of the Brillouin zone. The above-mentioned occurrence of three distinct sets of mirror (glide) planes in the NiSe (CoSe) crystal structure protects the nodal lines in the Brillouin zone. In the $k_1 = \pi$ plane, a single diamond-shaped nodal line exists (Figure 1d), while, in the $k_3 = 0$ plane, two distinct types of nodal lines, one encircling the Γ point and another encircling the K point, occur (Figure 1e). The nodal line around Γ respects the sixfold rotation symmetry, while the nodal lines around K have threefold rotational symmetry (Figure 1e). Interestingly, all nodal lines are interlinked with each other, and they form a unique chainlike nodal-link structure.

Based on the peculiar band structure of NiSe and CoSe, we calculated their corresponding macroscopic dynamical dielectric functions using time-dependent density functional theory. Note that both NiSe and CoSe are uniaxial crystals (i.e., the in-plane and out-of-plane dielectric permittivities $\varepsilon_{\parallel}$ and $\varepsilon_{\perp}$ are different). The calculated dielectric functions are shown in Figure 1f,g for NiSe and Figure S1 in the Supporting Information for CoSe, respectively. Owing to their similar crystal and metallic band structure (Figure 1c,d), correspondingly, the dielectric function of both materials behaves similarly. Both materials display a giant electromagnetic anisotropy, even with a hyperbolic response (i.e., the real parts of the in-plane and out-of-plane dielectric permittivity have opposite sign) in some parts of the spectrum.

In the assessment of the dependence of the light-to-heat conversion on NP size, one should consider that the absorption process is efficient only whenever the NP size is smaller than the corresponding skin depth = $\lambda/(2\ \pi\ \mathrm{Im}\ n)$, where n is the average of the in-plane and out-plane components of the NP refractive index and λ is the wavelength. As a matter of fact, when the light illuminates a metallic NP, a part of the incoming photons is scattered by NP, while the remaining part is absorbed. For the cases of NiSe and CoSe, we can assert that the light-to-heat conversion efficiency is maximized in the optical range for NP diameters ranging from 20 to 50 nm.

Before implementing a technological validation of our model, we also assessed the light-to-heat conversion of NiSe and CoSe NPs loaded as nanofillers in nanocomposite systems, taking as a case-study example the specific application in desalination technology extensively illustrated in Figure 5 and its related discussion. The effective optical response of the nanocomposite was

© 2022 The Authors. Small published by Wiley-VCH GmbH

evaluated by using an effective medium theory. Precisely, the effective dielectric function ε_{eff} of the nanocomposites was calculated using the Maxwell Garnett approximation,[48] based on the theoretical model validated[49]

$$\varepsilon_{\text{eff}} \simeq \varepsilon_{\text{h}} + 3f\varepsilon_{\text{h}} \frac{(\varepsilon_{\parallel}+2\varepsilon_{\text{h}})(\varepsilon_{\perp}-\varepsilon_{\text{h}}) - 2\varepsilon_{\text{h}}(\varepsilon_{\perp}-\varepsilon_{\parallel})}{(\varepsilon_{\parallel}+2\varepsilon_{\text{h}})(\varepsilon_{\perp}+2\varepsilon_{\text{h}})} \quad (1)$$

where f is the NP volume filling fraction, and ε_{h} is the dielectric permittivity of the host medium (in our case, PDMS, see Figure 5). It is important to note that, regardless the anisotropy of NiSe and CoSe, the resulting effective response of their nanocomposites is isotropic. Accordingly, it is described by a scalar dielectric permittivity and, thus, Equation (1) is related to a uniform orientation distribution.

Plasmonic resonances occur at either Re $\varepsilon_{\perp} = -2\varepsilon_{\text{h}}$ or Re $\varepsilon_{\parallel} = -2\varepsilon_{\text{h}}$, corresponding to the localized surface plasmon conditions of an anisotropic uniaxial sphere. The effective medium shows multiple surface plasmon resonances (**Figure 2**), unleashed by both the extreme anisotropy and the peculiar dielectric dispersion properties of NiSe and CoSe. The matching between surface plasmon resonances and sunlight radiation spectrum is beneficial for achieving an efficient plasmon-assisted solar thermal conversion.

To estimate the light-heat conversion efficiency of the nanocomposites, we considered the scattering of a monochromatic plane wave normally impinging onto a NP composite film embedded in vacuum. Solving Maxwell's equations, where the electromagnetic response of the nanocomposite is merely described by the effective dielectric permittivity, we analytically obtained the reflectivity (R) and the transmissivity (T). According to the energy conservation law, the absorption coefficient A is given by the equation $A = 1\text{-}R\text{-}T$. In Figure 2, we report the absorption coefficients as functions of the excitation energy and the volume filling fraction f for nanocomposite media with a) Ag, b) NiSe, and c) CoSe nanofillers. Remarkably, the considered nanocomposites support several surface plasmons (labeled by dashed white lines in Figure 2). In the NiSe-based nanocomposite, the surface plasmon resonance conditions occur at an energy of 3.09 eV ($\lambda = 0.40$ µm) corresponding to Re $\varepsilon_{\perp} = -2\varepsilon_{\text{h}}$ and, moreover, at 3.26 eV ($\lambda = 0.38$ µm) for which Re $\varepsilon_{\parallel} = -2\varepsilon_{\text{h}}$. In the CoSe-based nanocomposite, Re $\varepsilon_{\parallel} = -2\varepsilon_{\text{h}}$ is only satisfied for an energy of 3.02 eV ($\lambda = 0.41$ µm), whereas Re $\varepsilon_{\perp} = -2\varepsilon_{\text{h}}$ is fulfilled for 2.23, 2.75, and 3.02 eV ($\lambda = 0.56$, 0.45, and 0.41 µm, respectively).

Notably, silver nanofillers only exhibit a distinct surface plasmon resonance at 3.19 eV (corresponding to $\lambda = 0.39$ µm), with a limited matching with the solar spectrum. On the contrary, for NiSe- and CoSe-based nanocomposites, the multiple surface plasmons provide a broadband absorption, as reported in Figure 2b,c, nicely matching with the spectrum of sunlight radiation. In Section S9 (Supporting Information), we also directly compare the behavior of the Joule number (figure of merit for photothermal conversion introduced[50]) for Ag, NiSe, and CoSe in the optical range, where Ag is evidently less efficient in light-to-heat conversion.

However, the implementation of NiSe- and CoSe-based applications requires additional information on i) the stability of their hexagonal closed packed (hcp) crystalline structure and ii) their oxidation resistance.

In the bulk, layered hcp structures (Section S3, Supporting Information) of both NiSe and CoSe are more energetically favorable than the rhombohedral structure (Figure S2, Supporting Information). On the other hand, the surface energy, defined as the difference between total energy of slab (Figure S2, Supporting Information) and bulk, has a much smaller magnitude for rhombohedral than for hcp structures (see **Table 1**). Hence, in the case of NP of smaller size (<10 nm), when the contribution from surface areas in total energies is compatible with contribution from bulk areas, rhombohedral phases can also be realized, with two different surface terminations.

Moreover, we computed the energetics for the reactivity of the surfaces of hcp-NiSe and -CoSe toward oxygen adsorption and its subsequent decomposition, with resulting surface oxidation. In the case of hcp-NiSe, the decomposition of oxygen molecules (Figure S2d, Supporting Information) would be

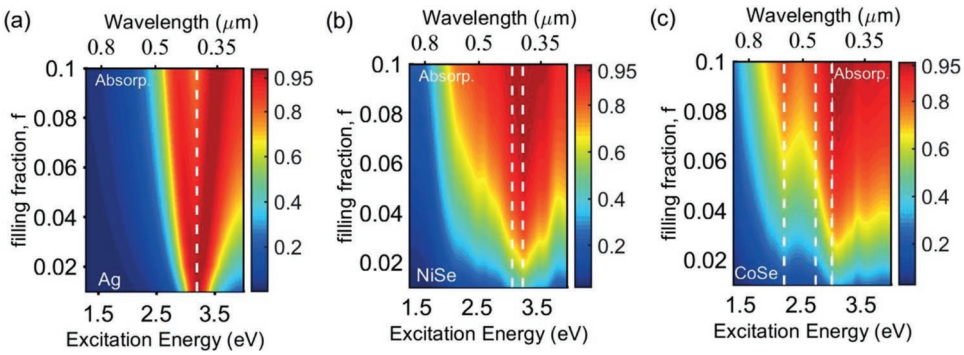

Figure 2. The absorption coefficients of the nanocomposite films (NPs embedded in a porous PDMS layer with a thickness of 1 µm) as a function of the excitation energy and the NP volume filling fraction f. We compare the cases of nanocomposites with a) Ag, b) CoSe, and c) NiSe NPs. The effective optical response of nanocomposites is described by considering the effective dielectric function ε_{eff} of Equation (1), where the host dielectric material ε_{h} is evaluated by using the standard Bruggeman's method,[45] i.e., $(1-f_{\text{p}})\frac{\varepsilon_{\text{v}}-\varepsilon_{\text{h}}}{\varepsilon_{\text{v}}+2\varepsilon_{\text{h}}} + f_{\text{p}}\frac{\varepsilon_{\text{p}}-\varepsilon_{\text{h}}}{\varepsilon_{\text{p}}+2\varepsilon_{\text{h}}} = 0$ with ε_{v} ($\varepsilon_{\text{v}} = 1$), ε_{p} are the vacuum and PMDS relative dielectric constants, respectively, and f_{p} is the PMDS volume filling fraction ($f_{\text{p}} = 0.43$). The PMDS and silver dielectric permittivity are given by the Sellmeier equation,[46] and a Lorentz–Drude model fitting the experimental data,[47] respectively. Dashed lines mark the spectral position of localized surface plasmon resonances.

© 2022 The Authors. Small published by Wiley-VCH GmbH

Table 1. Relative formation energies of bulk (E_{bulk}) rhombohedral (Rhomb) and hexagonal close-packed (hcp) phases of NiSe and CoSe (ground state set as zero); formation energies of the surfaces (E_{surf}) for all considered structures; differential enthalpies and the differential Gibbs free energies of physical adsorption (Figure S1a,b, Supporting Information); and differential enthalpies of oxygen decomposition (ΔH_{dec}, Figure S2c,d, Supporting Information). The formation of single and double oxygenated layers is also reported (ΔH_{O1}, Figure S2e,f and ΔH_{O2}, Figure S2i,j in the Supporting Information, respectively). All values are reported in kJ mol^{-1}. Negative values correspond to exothermic processes.

Compound	Structure	E_{bulk}	E_{surf}	Physisorption		ΔH_{dec} [kJ mol^{-1}]	ΔH_{O1} [kJ mol^{-1}]	ΔH_{O2} [kJ mol^{-1}]
				ΔH [kJ mol^{-1}]	ΔG [kJ mol^{-1}]			
NiSe	Rhomb-Se Rhomb-Ni	19.07	5.18	−32.90 −72.22	−21,41 −60,73	−138.46 −282.20	64.19 −176.44	128.46 21.49
	Hcp	0	28.68	6.19	17.68	−155.57	5.04	−41.25
CoSe	Rhomb-Se Rhomb-Co	19.56	−1.51	21.06 −100.61	32,55 −89.12	−42.89 −443.57	1178.24 1339.96	−126.48 −198.31
	hcp	0	20.68	−39.47	−27.98	−40.02	−0.41	0.84

energetically favorable, but molecular physisorption (Figure S2b, Supporting Information) is unfavorable (+17.68 kJ mol^{-1}). Congruently, dissociative adsorption can occur only at temperatures above 100 °C. Further oxidation of the hcp-NiSe surface (Figure S2f, Supporting Information) is unfavorable, although the energy cost of this process is rather moderate (only 5 kJ mol^{-1}) and even smaller than the energy gain from further oxidation (−41.25 kJ mol^{-1}). One can conclude that only partial oxidation of NiSe NP surface is energetically feasible at room temperature. This spot-like oxidation is expected to be localized just at defect-rich areas, such as steps, edges, and grain boundaries. The oxidation of the whole surface could be possible only after heating at a temperature above 100 °C, leading to the formation of limited oxidized skin over the surface (Figure S2i, Supporting Information), so that photothermal applications with operational temperature below 100 °C would operate with minimal surface oxidation rate and appropriate thermal stability.

In the case of hcp-CoSe, uniform oxygenation of defects-free surface layer (Figure S2j, Supporting Information) is possible even at room temperature, as indicated by the differential free energy of oxygen decomposition $\Delta H_{dec} = -40.02$ kJ mol^{-1}, although it is worth noticing that the formation of a thick oxide Co_3O_4 skin is limited by the reachability of subsurface Co atoms, with a resulting unfavorability already for a bilayer oxide thickness, with an energy barrier of 0.84 kJ mol^{-1}.

Theoretical predictions were validated experimentally. NiSe and CoSe NPs were synthetized following the Experimental Section extensively described in the corresponding section. The analysis of X-ray diffraction (XRD) pattern indicated that the crystallographic structure for both NPs is hcp ($P6_3/mmc$ space group), with lattice parameters matching with ICDD 00-002-0892 and 00-008-0414 for NiSe and CoSe, respectively. The analysis based on transmission electron microscopy (TEM) images (see histograms in Figure S3, Supporting Information) indicated a wide size distribution of synthetized NiSe and CoSe NPs (**Figure 3**a,b), with an average diameter of 30 ± 7 and 15 ± 5 nm for NiSe and CoSe NPs, respectively.

The physicochemical properties of NiSe and CoSe nanofillers, including their surface status, were assessed by nanospectroscopy tools at the soft X-ray beamline Nanospectroscopy at Elettra–Trieste synchrotron, using an energy-filtered Low Energy Electron Microscope (LEEM)-Photoelectron Emission Microscope (PEEM) with spatial resolution of 10 nm. Using X-ray photoelectron microscopy (XPEEM), NiSe and CoSe NPs were imaged (see Section S8, Supporting Information) and, moreover, core levels were acquired (Figure 3e) with nanoscale resolution. To provide information on the surface of the NPs, surface sensitivity was enhanced by using low-energy photons (150 eV). Specifically, we observed by μ-XPS (X-ray photoelectron spectroscopy) three different oxidation status in Se-3d core levels, arising from Se(II) and Se(0) species at a binding energy of 53.8 and 55.2 eV, respectively. On the other hand, oxidation is limited, as indicated by the SeO_{2-x} component at 58.0 eV with only 11% of the spectral area, while in previous studies on NiSe NPs this component was even predominant in the region of Se-3d core levels.[51] Conversely, the bulk crystals of the NPs are stoichiometric, as also indicated by the excellent matching of the experimental Ni-L_{23} absorption edge with theoretical predictions for the case of NiSe by using Feff 9 code.[52]

To validate the use of NiSe and CoSe NPs in thermoplasmonics, we implemented solar-driven MD with nanocomposite membranes with NiSe and CoSe nanofillers (see the Experimental Section for details on their fabrication). The SEM cross-sectional micrograph of the nanocomposite membrane (**Figure 4**a), made of a polyvinylidene fluoride (PVDF) support coated with a thin porous polydimethylsiloxane $(C_2H_6OSi)_n$ (PDMS) layer embedding NiSe or CoSe NPs, revealed a porous structure, which extends throughout the membrane thickness (180 ± 2 μm). The choice of PDMS as an anchoring agent for NPs secured a proper adhesion to the substrate, owing to the abundance of silanol moieties able to interact with the fluorinated support.[53] The coating layer appeared uniformly distributed over the PVDF support with a thickness of around 2 μm (Figure 4b). NPs are clearly noticeable on the surface of the composite membrane (Figure 4c), endowing the membrane with photothermal features. Noteworthy, the low concentration of Si in the sprayed solution secured an appropriate membrane porosity of the photothermal layer (i.e., 54.6 ± 1.6%), slightly lower than that of the bare support (56.7 ± 0.8%). This morphology, characterized by a mean pore size of 0.21 ± 0.05 μm, offers a minimal resistance to the mass transport of water vapor through the membrane.

Further characterization (Table S1, Supporting Information) confirmed that the developed nanocomposite membranes exhibited suitable features for MD applications. In particular, the high hydrophobic behavior (contact angle > 110°), combined with the submicrometric pore size (largest pore <0.3 μm), secures a Liquid Entry Pressure (LEP)—estimated according to the Young–Laplace equation[54]—ranging from 1.5 bar for 2.5 wt% CoSe-PDMS to 2.6 bar for 2.5 wt% NiSe-PDMS

© 2022 The Authors. Small published by Wiley-VCH GmbH

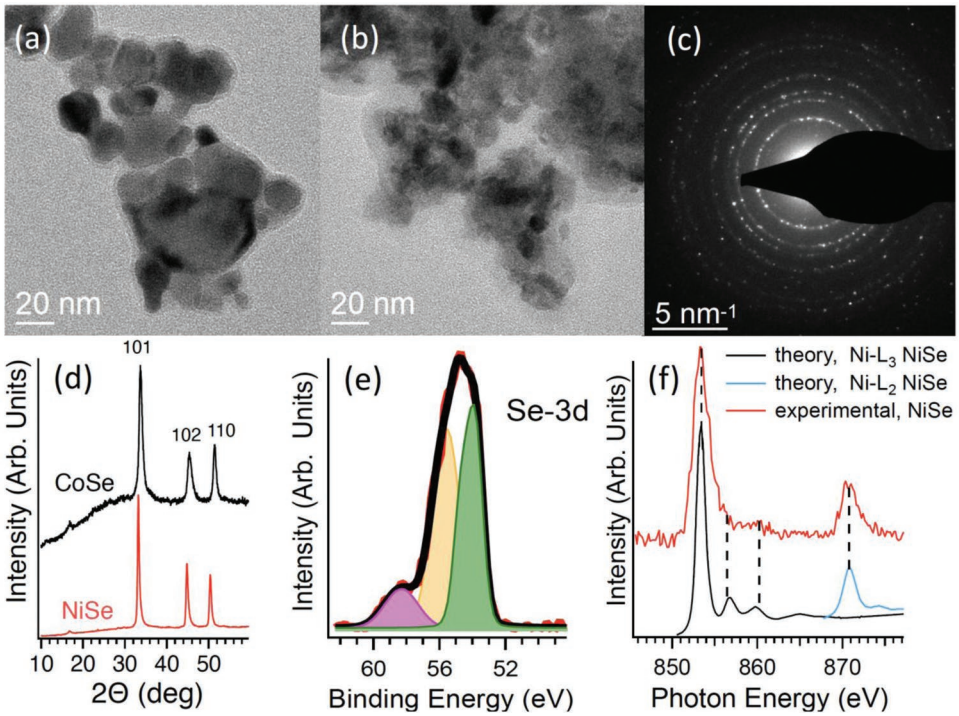

Figure 3. a) TEM images of NiSe b) and CoSe. c) SAED images of NiSe. d) Powder XRD diffraction pattern of NiSe and CoSe. e) μ-XPS spectrum on an individual NiSe NP (see Section S8, Supporting Information) measured by means of XPEEM apparatus, with a photon energy of 150 eV. The purple, yellow, and green areas depict the spectral contribution from SeO_{2-x}, Se(0) and Se(II) species, respectively. f) Experimental Ni-L_{23} absorption edge, measured on an individual NiSe NP (red spectrum, see Section S8 in the Supporting Information for XPEEM images), compared with theoretical predictions by Feff 9 code for L_2 and L_3 absorption edges of NiSe.

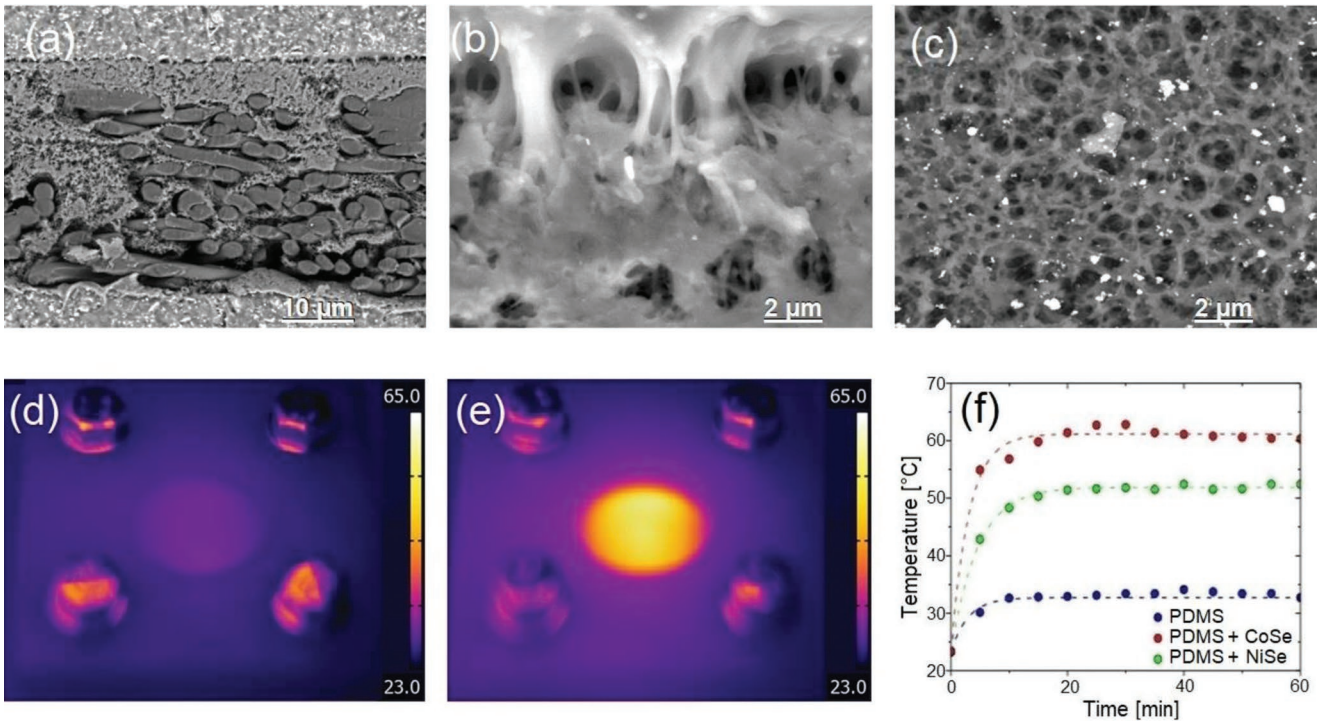

Figure 4. SEM micrographs of CoSe (2.5 wt%) in PDMS/PVDF membrane: a) cross-sectional view (magnification 900x). b) Detail of the cross-section of the coating (magnification 10 000x). c) Top view of coated surface (magnification 4000x). Infrared pictures under 1-sun illumination of composite membranes coated by d) bare PDMS and e) PDMS loaded with 2.5 wt% CoSe. f) Evolution in time of the temperature profile of membrane surface under solar radiation of bare PDMS coating and of nanocomposite coatings based on 2.5 wt% of NiSe and CoSe embedded into PDMS.

© 2022 The Authors. Small published by Wiley-VCH GmbH

(Section S5, Supporting Information). The values of LEP, i.e., the minimum hydrostatic pressure required to push the liquid into the largest membrane pores, exceeded the operational transmembrane pressure of vacuum membrane distillation (VMD) process (ΔP = 1.05 bar), preventing the wetting phenomenon and the consequent reduction of the salt rejection.[55]

Energy-dispersive X-ray spectroscopy (EDS) analysis revealed the presence of Si atoms only within the coated top layer (Figure S4a, Supporting Information). This observation was corroborated by cross-sectional EDS analysis of the membranes with PDMS coatings loaded with 2.5 wt% NiSe (Figure S4b, Supporting Information) and 2.5 wt% CoSe (Figure S4c, Supporting Information), which confirmed the presence of metallic NPs in the proximity of the membrane surface. This is a crucial aspect, since the localization of NPs at the membrane surface: i) secures an efficient absorption of the incident radiation; ii) accelerates the evaporation rate thanks to an efficient light-to-heat conversion at the membrane-water interface, and iii) minimizes the cost of the nanocomposite photothermal layer.[56]

Thermal imaging upon solar irradiation (Figure 4d,e; and Figure S5, Supporting Information) revealed the effectiveness of light-to-heat conversion promoted by the plasmonic nanofillers. Interestingly, the coating with 2.5 wt% CoSe (NiSe) coating reached a temperature of 61.9 ± 0.5 °C (52.4 ± 0.5 °C) under the equivalent of 1-sun solar irradiance (1000 W m^{-2}) in about 10 min (Figure 4f). On the contrary, without photothermal nanofillers, i.e., for the bare PDMS coating, a temperature of 32.7 ± 0.5 °C was observed even after 1 h of sunlight exposure.

This efficient light-to-heat conversion localized on the membrane surface is very attractive for the MD process, securing a sustainable energy harvesting for the interfacial evaporation of water molecules and an effective overcoming of the thermal polarization, the major drawback of MD technology.[20] Therefore, the self-heating properties of the photothermal membranes are exploitable for boosting the vaporization of water: CoSe coating demonstrated a superior light-to-heat-to vapor conversion with a photothermal efficiency (η) of 54.2%; whereas values of 18.4% and 38.3% were observed for bare PDMS and PDMS loaded with 2.5 wt% NiSe coating, respectively.

More precisely, we tested the potential of NiSe and CoSe for thermoplasmonics by implementing a solar-driven VMD. It should be remembered that in VMD the transmembrane flux (J_w) is proportional to the difference between the partial pressure of water vapor at the feed-membrane interface ($p_w^{membrane}$) and the vacuum pressure (p_w^{vacuum})

$$J_w = K\left(p_w^{membrane} - p_w^{vacuum}\right) \tag{2}$$

where $\left(p_w^{membrane} - p_w^{vacuum}\right)$ represents the driving force for the transport of water molecules in the gas phase through the membrane, and K is the mass transfer coefficient. According to Raoult's law, the value of $p_w^{membrane}$ is obtained by multiplying the vapor pressure of pure water p_w^0 evaluated at the interface temperature of the membrane (T_f^*), the molar fraction (x_w) and activity coefficient (γ_w, ≠1 for a nonideal mixture) of water in the feed solution.

The presence of photothermal NPs in the polymeric coating negligibly impacted on K. Membranes with a coating of bare PDMS and its modification by the inclusion of 2.5 wt% NiSe and CoSe nanofillers exhibited K values of 55.2, 58.1, and 58.9 kg m^{-2} h^{-1} atm^{-1} respectively, as resulting from VMD experiments carried out at 20 °C without sunlight irradiation.

The advantages of the efficient light-to-heat conversion of NiSe and CoSe NPs are evident from the inspection of **Figure 5**. The temperature increase generated by nanoscale thermal hotspots resulted in an exponential increase of the transmembrane flux (J_w), coherently with the trend of water vapor pressure established by the Clausius–Clapeyron equation ($p_w^{membrane}$ increased from 39 to 152 mmHg under artificial solar irradiation sun by embedding CoSe NPs).

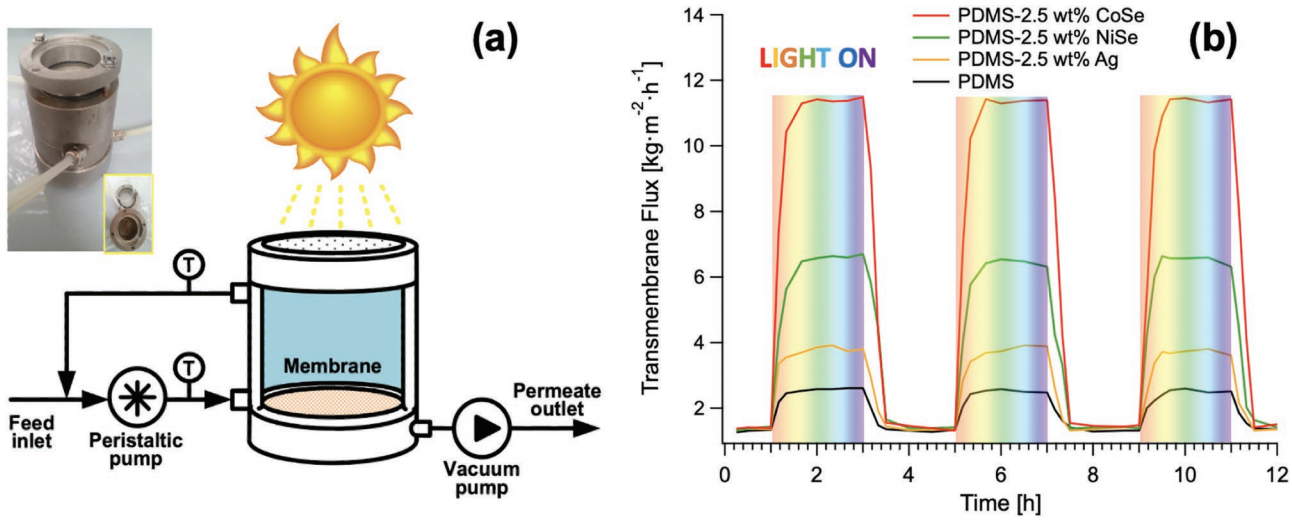

Figure 5. a) Schematics of solar-driven VMD. The inset shows a photograph of the experimental apparatus. b) Transmembrane flux in VMD experiments using composite membranes with a coating of (black curve) bare PDMS and, moreover, 2.5 wt% of (orange curve) Ag; (green curve) NiSe; and (red curve) CoSe NPs embedded into PDMS. Feed: artificial seawater (0.5 M NaCl). Experiments were repeated for three cycles covering 12 h in presence (light ON) or absence (light OFF) of artificial solar irradiation (1000 W m^{-2}).

© 2022 The Authors. Small published by Wiley-VCH GmbH

For VMD operating under 1-sun illumination with pure water at 20 °C, bare PDMS coating provided a J_w of 2.6 ± 0.13 kg m^{-2} h^{-1} (T_f^* = 32.7 °C), whereas the evaporative flux raised to 6.8 ± 0.3 and 11.4 ± 0.3 kg m^{-2} h^{-1} in the presence of NiSe and CoSe nanofillers (corresponding to T_f^* of 52.4 and 61.9 °C), respectively. Moreover, the improvement of the productivity of the VMD process without increasing the energetic input resulted in a decreasing of the Specific Thermal Energy Consumption (STEC) required for water vaporization. In fact, the embodiment of NiSe and CoSe reduced the STEC of VMD of 61.8% and 77.2%, respectively, in comparison to the bare PDMS coating. The STEC required for solar-driven VMD performed with photothermal membranes load with CoSe nanofillers was 80 Kwh m^{-3} below the range of 130–210 Kwh m^{-3} estimated for stand-alone pilot-plant supplied by Solar Photovoltaic Technology.[57]

The effectiveness of desalination operations was confirmed by VMD experiments performed by feeding both seawater (0.5 M NaCl) and seawater reverse osmosis brine (1.0 M NaCl). Regardless of the concentration of dissolved salt, a high-quality distilled water (electrical conductivity below 0.1 µS cm^{-1}) was collected as permeate. Moreover, the transmembrane flux (Figure S6, Supporting Information) only showed a slight decrease by 4.3% and 5.2% when increasing the feed solution concentration to 0.5 and 1 M, respectively, due to the diminution of γ_w (from 0.983 to 0.966) and x_w (0.991–0.981).

In Figure 5b, we also compare NiSe and CoSe with state-of-the-art reference for photothermal MD, i.e., Ag under 1-sun illumination. Notably, replacing Ag with NiSe and CoSe for solar membrane distillation increases of the transmembrane flux by 330% and 690%, respectively. Correspondingly, costs are reduced by 24 and 11 times, respectively. Moreover, the fabricated NiSe- and CoSe-based nanocomposite membranes are exceptionally stable, as demonstrated by the excellent reproducibility even for an extended amount of working hours, consistently with the suitable chemical stability of NiSe and CoSe nanofillers inferred by density functional theory (Table 1) and µ-XPS data (Figure 3e).

Both DLS and high-resolution continuum source atomic absorption spectrometer (HR-CS AAS) analysis proved the absence of NiSe or CoSe NPs and related ions in the distillate, which presented in all cases a conductivity below than 10 µS cm^{-1}, demonstrating the efficiency of the photothermal membrane in seawater desalination (ion rejection>99%) and the absence of leaching.

The long-term stability of the photothermal membrane was demonstrated by protracting photothermal VMD practices for 24 h (Figure S11 in the Supporting Information). VMD experiments using composite membranes with a coating of PDMS loaded with 2.5 wt% of CoSe secured a recovery factor of ≈75% in 24 h leading to a significant improvement of the concentration of NaCl in the retentate from 0.5 to 2 M reducing therefore the driving force of the mass transport due to the due to the diminution of γ_w (from 0.983 to 0.923) and x_w (0.991–0.965) (see Equation (2)). Hence, the implementation of CoSe in solar-driven VMD favors a drastic reduction of the brine produced in the retentate as byproduct of the process. Noteworthy, these experiments confirmed the opportunity to intensify the desalination process via solar-driven VMD exceeding the current water recovery factor of 50% of traditional desalination based on Reverse Osmosis.

Finally, the biofouling resistance of the hydrophobic polymeric membrane is discussed in Section S12 of the Supporting Information.

In conclusion, the promising prospect of NiSe and CoSe for thermoplasmonics has been demonstrated by a joint theoretical and experimental investigation, going from the disclosure of their exotic electronic and optical properties up to technological implementation in the field of solar desalination. Remarkably, NiSe and CoSe show a giant electromagnetic anisotropy enabling multiple localized surface plasmon resonances lying in the optical range, as well as an unprecedentedly efficient plasmon-assisted solar thermal conversion. To validate our model, we carried out experiments of solar membrane distillation, using NiSe and CoSe NPs synthetized for this aim with a size tuned for achieving the optimal light-to-heat conversion efficiency. Explicitly, replacing Ag with NiSe and CoSe for solar MD increased the transmembrane flux by 330% and 690%, respectively, and, in addition, the corresponding costs of raw materials are reduced by 24 and 11 times. Accordingly, already in the first implementation, NiSe- and CoSe-based solar desalination largely exceeds state-of-the-art performances. Evidently, photothermal effects in NiSe and CoSe can improve the efficiency of any other application based on solar thermal conversion (solar steam generation, high-temperature heterogeneous catalysis, solar thermophotovoltaics, thermoelectric power generation, etc.), beyond solar-driven MD herein selected as a case-study example.

Finally, it is noteworthy to highlight that NiSe and CoSe also exhibit unusual topological electronic states and optical features (viz., multiple topological Dirac nodal-line structures and hyperbolic electromagnetic response), bringing exciting new perspectives in the field of nanophotonics and topological materials.

Experimental Section

Synthesis of NiSe and CoSe NPs: NiSe and CoSe NPs were synthesized by a solvothermal technique. The initial step for the synthesis of NiSe and CoSe consisted in dissolving nickel (II) nitrate hexahydrate $Ni(NO_3)_2 \cdot 6H_2O$ (0.2 mmol) and cobalt (II) nitrate hexahydrate $Co(NO_3)_2 \cdot 6H_2O$ (0.2 mmol) in 50 mL of deionized water with stirring for 10 min, respectively. Separately, selenium powder (0.4 mmol) and hydrazine hydrate (20 mL) were stirred for 10 min. The two solutions were mixed and transferred to a Teflon-lined stainless-steel autoclave containing ethanolamine (10 mL) and kept at 180 °C for 16 h. After cooling to room temperature, the obtained products were centrifuged, washed several times with ethanol, and dried under vacuum.

Instrumentation and Methods: *TEM*: The suspensions were drop-casted onto a TEM grid and dried. JEOL 2100F transmission electron microscope operated at 200 kV.

SEM: Field emission scanning electron microscope (FESEM) experiments were carried with Gemini SEM 500, at an accelerating voltage of 2 kV.

Powder XRD: Panalytical Empyrean powder X-ray diffractometer equipped with a position-sensitive X'Celerator detector using Cu kα radiation.

Porometer: Measurements of pore size of nanocomposite membranes were carried out by using a PMI capillary flow porometer (Porous Materials Inc., Ithaca, NY) using Porewick (surface tension = 16 dyn cm^{-1}) as wetting liquid and processing the data with the software Caprep (Porous Materials Inc., Ithaca, NY).

© 2022 The Authors. Small published by Wiley-VCH GmbH

Membrane Preparation: Composite membranes based on a thin porous layer of PDMS (Sigma-Aldrich) loaded with NiSe and CoSe NPs were prepared by the spray coating method. As support, a microporous commercial PVDF membrane Fortex complying ISO 10 993 and USP Class VI, with nominal pore size 0.2 µm (GVS, Italy) was used. The coating solution was prepared by dispersing the photothermal NPs via sonication (Sonica2200ETH, Soltec, Italy) for 30 min in heptane (Sigma-Aldrich). Then, PDMS was dissolved into the colloidal solution (5 wt%) by stirring for 3 h at room temperature. The concentration of the photothermal NPs was 2.5 wt% with respect to PDMS. Finally, the crosslinker was added to the polymeric solution at a concentration of 10 wt% with respect to PDMS. The polymeric solution (10 mL) was then transferred to an airbrush equipped with a compressor (Gocheer, model TS100BMC). The system was mounted on a 2D positioning control system for the planar motion (TEVO Tornado) at a velocity 60 mm s^{-1}. Each PVDF membrane (112 cm^2) was sprayed three times and then transferred in an oven at 60 °C for 60 min to promote the crosslinking of the polymer and the evaporation of the solvent.

VMD Experiments: A solar irradiation simulator (Abet Technologies, US) with irradiance of 1 sun (1000 W m^{-2}) over a 35 mm diameter field was used to irradiate a dedicated dead-end VMD cell with effective membrane area of 7.06 cm^2. The VMD cell was equipped with a quartz window and the solar lamp was put 10 cm above this quartz window to ensure that the light could irradiate the membrane. Feed solution recirculated throughout the cell at 5.5×10^{-6} m^3 s^{-1} by using a peristaltic pump (VWR VP 820). The lab-scale plant operated under vacuum pressure of 20 mbar and initial feed temperature of 293 K. The permeate conductivity was measured using a YSI Model 3200 conductivity meter at 20 °C (range: 0–4999 µS m^{-1}, accuracy: ±0.50% full scale, resolution: 1 µS m^{-1}). For solar-driven VMD experiments, experiments with the same Ag NPs used for the previous works[10c,d] for the sake of comparison were also carried out.

Feed solution recirculated throughout the cell at 5.5×10^{-6} m^3 s^{-1} by a Masterflex L/S digital peristaltic pumps (Cole-Palmer, US), whereas distillate was stripped by a vacuum pump VWR VP 820 (VWR International, US).

The quality of the distillate was estimated with a DLS 90Plus Particle Size Analyzer (Brookhaven Instruments Corporation, USA) and a HR-CS AAS by means of ContrAA 700 (Analytik Jena AG, Germany) with a high-intensity Xe short-arc lamp as continuum source.

STEC of solar-driven VMD was estimated according to the following equation

$$\mathrm{STEC} = \frac{P\rho}{J} \tag{3}$$

where P is the irradiance of the artificial sunlight, ρ is the water density, and J is the transmembrane flux in VMD practice.

Supporting Information

Supporting Information is available from the Wiley Online Library or from the author.

Acknowledgements

S.A., D.D., C.R., and S.S. contributed equally to this work. D.W.B. thanks the Jiangsu Innovative and Entrepreneurial Talents Project. This work has been partially supported by the Spanish Ministerio de Ciencia e Innovación under Project No. PID2019–109525RB-I00. D.F. acknowledges financial support from the Spanish Ministry of Economy and Competitiveness, through the "María de Maeztu" Programme for Units of Excellence in R&D (No. CEX2018-000805-M). S.S. acknowledges the European Commission through the PON "Research and Innovation" 2014-2020. Action I.2 "Researchers' Mobility". Notice D.D. 407 of 02.27.2018 - AIM "Attraction and International Mobility"-Line 2 "Researchers' Attraction".

Open access funding provided by Universita degli Studi dell'Aquila within the CRUI-CARE Agreement.

Conflict of Interest

The authors declare no conflict of interest.

Data Availability Statement

The data that support the findings of this study are available from the corresponding author upon reasonable request.

Keywords

solar membrane distillation, thermoplasmonics, topological materials, optical anisotropy, nodal-line semimetals

Received: March 7, 2022
Revised: April 26, 2022
Published online: July 9, 2022

[1] a) G. Baffou, F. Cichos, R. Quidant, *Nat. Mater.* **2020**, *19*, 946; b) Y. Liu, J. Liu, Q. Zhang, Q. Zhu, X. Liu, Z. Wang, Z. Dai, *Adv. Funct. Mater.* **2022**, *32*, 2106854; c) L. Uson, C. Yus, G. Mendoza, E. Leroy, S. Irusta, T. Alejo, D. García-Domingo, A. Larrea, M. Arruebo, R. Arenal, V. Sebastian, *Adv. Funct. Mater.* **2022**, *32*, 2106932; d) Q. Yu, T. Peng, J. Zhang, X. Liu, Y. Pan, D. Ge, L. Zhao, F. Rosei, J. Zhang, *Small* **2022**, *18*; e) Q. Xiang, C. Yang, Y. Luo, F. Liu, J. Zheng, W. Liu, H. Ran, Y. Sun, J. Ren, Z. Wang, *Small* **2022**, *18*, 2107809; f) B. Shan, H. Liu, L. Li, Y. Lu, M. Li, *Small* **2022**, *18*, 2105638.

[2] a) X. Liu, Y. Yang, M. Ling, R. Sun, M. Zhu, J. Chen, M. Yu, Z. Peng, Z. Yu, X. Liu, *Adv. Funct. Mater.* **2021**, *31*, 2101709; b) B. Tian, S. Liu, L. Feng, S. Liu, S. Gai, Y. Dai, L. Xie, B. Liu, P. Yang, Y. Zhao, *Adv. Funct. Mater.* **2021**, *31*, 2100549; c) P. Ye, F. Li, J. Zou, Y. Luo, S. Wang, G. Lu, F. Zhang, C. Chen, J. Long, R. Jia, M. Shi, Y. Wang, X. Cheng, G. Ma, W. Wei, *Adv. Funct. Mater.* **2022**, *32*, 2110063; d) R. Zheng, Q. Zhao, W. Qing, S. Li, Z. Liu, Q. Li, Y. Huang, *Small* **2022**, *18*, 2103174.

[3] Y. An, Y. Nam, *J. Neural Eng.* **2021**, *18*, 066002.

[4] Q. Bai, M. Liang, W. Wu, C. Zhang, X. Li, M. Liu, D. Yang, W. W. Yu, Q. Hu, L. Wang, F. Du, N. Sui, Z. Zhu, *Adv. Funct. Mater.* **2022**, *32*, 2112683.

[5] M. Sun, Z. Ji, L. He, C. Zhao, L. Ma, X. Xu, E. J. Cornel, Z. Fan, X. Xu, *Adv. Funct. Mater.* **2022**, *32*, 2107999.

[6] a) G. Qiu, Z. Gai, L. Saleh, J. Tang, T. Gui, G. A. Kullak-Ublick, J. Wang, *ACS Nano* **2021**, *15*, 7536; b) G. Qiu, Z. Gai, Y. Tao, J. Schmitt, G. A. Kullak-Ublick, J. Wang, *ACS Nano* **2020**, *14*, 5268.

[7] Z. Li, Z. Ye, L. Han, Q. Fan, C. Wu, D. Ding, H. L. Xin, N. V. Myung, Y. Yin, *Adv. Mater.* **2021**, *33*, 2006367.

[8] A. Naldoni, Z. A. Kudyshev, L. Mascaretti, S. P. Sarmah, S. Rej, J. P. Froning, O. Tomanec, J. E. Yoo, D. Wang, Š. Kment, T. Montini, P. Fornasiero, V. M. Shalaev, P. Schmuki, A. Boltasseva, R. Zbořil, *Nano Lett.* **2020**, *20*, 3663.

[9] a) L. Mascaretti, A. Schirato, R. Zbořil, Š. Kment, P. Schmuki, A. Alabastri, A. Naldoni, *Nano Energy* **2021**, *83*, 105828; b) Y. Lin, H. Xu, X. Shan, Y. Di, A. Zhao, Y. Hu, Z. Gan, *J. Mater. Chem. A*

© 2022 The Authors. Small published by Wiley-VCH GmbH

2019, *7*, 19203; c) X. Han, L. V. Besteiro, C. S. L. Koh, H. K. Lee, I. Y. Phang, G. C. Phan-Quang, J. Y. Ng, H. Y. F. Sim, C. L. Lay, A. Govorov, X. Y. Ling, *Adv. Funct. Mater.* **2021**, *31*, 2008904; d) H. Zhang, X. Shen, E. Kim, M. Wang, J. H. Lee, H. Chen, G. Zhang, J. K. Kim, *Adv. Funct. Mater.* **2022**, *32*, 2111794; e) M. S. Irshad, N. Arshad, X. Wang, H. R. Li, M. Q. Javed, Y. Xu, L. A. Alshahrani, T. Mei, J. Li, *Sol. RRL* **2021**, *5*, 2100427; f) M. S. Irshad, X. Wang, A. Abbas, F. Yu, J. Li, J. Wang, T. Mei, J. Qian, S. Wu, M. Q. Javed, *Carbon* **2021**, *176*, 313; g) M. S. Irshad, X. Wang, M. S. Abbasi, N. Arshad, Z. Chen, Z. Guo, L. Yu, J. Qian, J. You, T. Mei, *ACS Sustainable Chem. Eng.* **2021**, *9*, 3887; h) S.-L. Loo, L. Vásquez, M. Zahid, F. Costantino, A. Athanassiou, D. Fragouli, *ACS Appl. Mater. Interfaces* **2021**, *13*, 263.

[10] a) A. Politano, A. Cupolillo, G. Di Profio, H. Arafat, G. Chiarello, E. Curcio, *J. Phys.: Condens. Matter* **2016**, *28*, 363003; b) D. Elmaghraoui, A. Politano, S. Jaziri, *J. Chem. Phys.* **2020**, *152*, 114102; c) A. Politano, P. Argurio, G. Di Profio, V. Sanna, A. Cupolillo, S. Chakraborty, H. A. Arafat, E. Curcio, *Adv. Mater.* **2017**, *29*, 1603504; d) A. Politano, G. Di Profio, E. Fontananova, V. Sanna, A. Cupolillo, E. Curcio, *Desalination* **2019**, *451*, 192; e) Y. Z. Tan, H. Wang, L. Han, M. B. Tanis-Kanbur, M. V. Pranav, J. W. Chew, *J. Membr. Sci.* **2018**, *565*, 254.

[11] F. Leon, A. Ramos, J. Vaswani, C. Mendieta, S. Brito, *Water* **2021**, *13*, 293.

[12] L. Rosa, D. D. Chiarelli, M. C. Rulli, J. Dell'Angelo, P. D'Odorico, *Sci. Adv.* **2020**, *6*, eaaz6031.

[13] a) K. Hainsch, K. Löffler, T. Burandt, H. Auer, P. C. del Granado, P. Pisciella, S. Zwickl-Bernhard, *Energy* **2022**, *239*, 122067; b) M. S. Zafar, M. Zahid, A. Athanassiou, D. Fragouli, *Adv. Sustainable Syst.* **2021**, *5*, 2100031.

[14] a) N. Mir, Y. Bicer, *Desalination* **2021**, *499*, 114822; b) X. Su, D. Hao, M. Sun, T. Wei, D. Xu, X. Ai, X. Guo, T. Zhao, L. Jiang, *Adv. Funct. Mater.* **2022**, *32*, 2108135; c) Z. C. Xiong, Y. J. Zhu, Z. Y. Wang, Y. Q. Chen, H. P. Yu, *Adv. Funct. Mater.* **2022**, *32*, 2106978.

[15] a) A. Siefan, E. Rachid, N. Elashwah, F. AlMarzooqi, F. Banat, R. van der Merwe, *Desalination* **2022**, *522*, 115383; b) Q. Ma, Z. Xu, R. Wang, *Water Res.* **2021**, *198*, 117154.

[16] a) A. Ali, R. A. Tufa, F. Macedonio, E. Curcio, E. Drioli, *Renewable Sustainable Energy Rev.* **2018**, *81*, 1; b) H. Lu, W. Shi, F. Zhao, W. Zhang, P. Zhang, C. Zhao, G. Yu, *Adv. Funct. Mater.* **2021**, *31*, 2101036.

[17] a) E. Curcio, E. Drioli, *Sep. Purif. Rev.* **2005**, *34*, 35; b) I. Hitsov, T. Maere, K. De Sitter, C. Dotremont, I. Nopens, *Sep. Purif. Technol.* **2015**, *142*, 48.

[18] a) R. Miladi, N. Frikha, A. Kheiri, S. Gabsi, *Energy Convers. Manag.* **2019**, *185*, 143; b) Q. Li, L. J. Beier, J. Tan, C. Brown, B. Lian, W. Zhong, Y. Wang, C. Ji, P. Dai, T. Li, P. Le Clech, H. Tyagi, X. Liu, G. Leslie, R. A. Taylor, *Appl. Energy* **2019**, *237*, 534; c) A. Abdel-Karim, J. M. Luque-Alled, S. Leaper, M. Alberto, X. Fan, A. Vijayaraghavan, T. A. Gad-Allah, A. S. El-Kalliny, G. Szekely, S. I. A. Ahmed, S. M. Holmes, P. Gorgojo, *Desalination* **2019**, *452*, 196; d) L. García-Fernández, B. Wang, M. C. García-Payo, K. Li, M. Khayet, *Desalination* **2017**, *420*, 226; e) L. Eykens, I. Hitsov, K. De Sitter, C. Dotremont, L. Pinoy, B. Van der Bruggen, *Desalination* **2017**, *422*, 91.

[19] A. Matin, T. Laoui, W. Falath, M. Farooque, *Sci. Total Environ.* **2021**, *765*, 142721.

[20] A. Anvari, A. A. Yancheshme, K. M. Kekre, A. Ronen, *J. Membr. Sci.* **2020**, *616*, 118413.

[21] A. G. Razaqpur, Y. Wang, X. Liao, Y. Liao, R. Wang, *Water Res.* **2021**, *201*, 117299.

[22] a) H. Ye, X. Li, L. Deng, P. Li, T. Zhang, X. Wang, B. S. Hsiao, *Ind. Eng. Chem. Res.* **2019**, *58*, 3269; b) M. Gao, C. K. Peh, F. L. Meng, G. W. Ho, *Small Methods* **2021**, *5*, 2001200.

[23] G. V. Naik, V. M. Shalaev, A. Boltasseva, *Adv. Mater.* **2013**, *25*, 3264.

[24] Y. Li, C. Lin, Z. Wu, Z. Chen, C. Chi, F. Cao, D. Mei, H. Yan, C. Y. Tso, C. Y. H. Chao, B. Huang, *Adv. Mater.* **2021**, *33*, 2005074.

[25] D. B. O'Neill, S. K. Frehan, K. Zhu, E. Zoethout, G. Mul, E. C. Garnett, A. Huijser, S. H. C. Askes, *Adv. Opt. Mater.* **2021**, *9*, 2100510.

[26] J. Yang, L. Sun, S. Hui, P. Zhang, J. Li, D. Wang, X. Wang, S. Jiang, *Biomater. Sci.* **2021**, *9*, 4728.

[27] S. Lee, L. Truong, M.-J. Lee, S.-H. Chun, *Cryst. Growth Des.* **2021**, *21*, 6648.

[28] Z. Xie, Y. Duo, Z. Lin, T. Fan, C. Xing, L. Yu, R. Wang, M. Qiu, Y. Zhang, Y. Zhao, *Adv. Sci.* **2020**, *7*, 1902236.

[29] C. Liu, S. Sun, Q. Feng, G. Wu, Y. Wu, N. Kong, Z. Yu, J. Yao, X. Zhang, W. Chen, Z. Tang, Y. Xiao, X. Huang, A. Lv, C. Yao, H. Cheng, A. Wu, T. Xie, W. Tao, *Adv. Mater.* **2021**, *33*, 2102054.

[30] J. Ouyang, L. Zhang, L. Li, W. Chen, Z. Tang, X. Ji, C. Feng, N. Tao, N. Kong, T. Chen, *Nano-Micro Lett.* **2021**, *13*, 1.

[31] a) X. Fan, Y. Ding, Y. Liu, J. Liang, Y. Chen, *ACS Nano* **2019**, *13*, 8124; b) K. Chaudhuri, M. Alhabeb, Z. Wang, V. M. Shalaev, Y. Gogotsi, A. Boltasseva, *ACS Photonics* **2018**, *5*, 1115.

[32] a) E. Sachet, C. T. Shelton, J. S. Harris, B. E. Gaddy, D. L. Irving, S. Curtarolo, B. F. Donovan, P. E. Hopkins, P. A. Sharma, A. L. Sharma, *Nat. Mater.* **2015**, *14*, 414; b) K. Sun, W. Xiao, S. Ye, N. Kalfagiannis, K. S. Kiang, C. de Groot, O. L. Muskens, *Adv. Mater.* **2020**, *32*, 2001534; c) Y. Wang, A. C. Overvig, S. Shrestha, R. Zhang, R. Wang, N. Yu, L. Dal Negro, *Opt. Mater. Express* **2017**, *7*, 2727; d) A. Shabani, M. K. Nezhad, N. Rahmani, Y. K. Mishra, B. Sanyal, J. Adam, *Adv. Photonics Res.* **2021**, *2*, 2000086.

[33] J. O. Island, G. A. Steele, H. S. J. van der Zant, A. Castellanos-Gomez, *2D Mater.* **2015**, *2*, 011002.

[34] V. Paolucci, G. D'Olimpio, C. N. Kuo, C. S. Lue, D. W. Boukhvalov, C. Cantalini, A. Politano, *ACS Appl. Mater. Interfaces* **2020**, *12*, 34362.

[35] a) M. B. Cortie, M. D. Arnold, V. J. Keast, *Adv. Mater.* **2020**, *32*, 1904532; b) T. Gong, J. N. Munday, *Opt. Mater. Express* **2015**, *5*, 2501.

[36] a) A. Rasmussen, T. Deilmann, K. S. Thygesen, *npj Comput. Mater.* **2021**, *7*, 22; b) Y. Xu, L. Elcoro, Z.-D. Song, B. J. Wieder, M. Vergniory, N. Regnault, Y. Chen, C. Felser, B. A. Bernevig, *Nature* **2020**, *586*, 702.

[37] A. Jain, S. P. Ong, G. Hautier, W. Chen, W. D. Richards, S. Dacek, S. Cholia, D. Gunter, D. Skinner, G. Ceder, *APL Mater.* **2013**, *1*, 011002.

[38] a) C. Wang, G. Zhang, S. Huang, Y. Xie, H. Yan, *Adv. Opt. Mater.* **2020**, *8*, 1900996; b) A. Nemilentsau, T. Low, G. Hanson, *Phys. Rev. Lett.* **2016**, *116*, 066804.

[39] K. Korzeb, M. Gajc, D. A. Pawlak, *Opt. Express* **2015**, *23*, 25406.

[40] S. Zhang, W. Shi, T. D. Siegler, X. Gao, F. Ge, B. A. Korgel, Y. He, S. Li, X. Wang, *Angew. Chem.* **2019**, *131*, 8822.

[41] H. Yang, H. Jussila, A. Autere, H.-P. Komsa, G. Ye, X. Chen, T. Hasan, Z. Sun, *ACS Photonics* **2017**, *4*, 3023.

[42] R. Dehbashi, K. S. Bialkowski, A. M. Abbosh, *J. Appl. Phys.* **2017**, *121*, 203103.

[43] Y. Song, V. Tran, J. Lee, *ACS Appl. Mater. Interfaces* **2017**, *9*, 24433.

[44] X. Zhang, L. Guo, B. Zhang, J. Yu, Y. Wang, K. Wu, H.-j. Wang, M.-H. Lee, *Chem. Commun.* **2021**, *57*, 639.

[45] D. A. G. Bruggeman, *Ann. Phys.* **1935**, *416*, 636.

[46] F. Schneider, J. Draheim, R. Kamberger, U. Wallrabe, *Sens. Actuators, A* **2009**, *151*, 95.

[47] B. Ung, Y. Sheng, *Opt. Express* **2007**, *15*, 1182.

[48] L. Landau, E. Lifshitz, L. Pitaevskii, *Electrodynamics of Continuous Media*, Pergamon Press, Oxford **1984**.

[49] O. Levy, D. Stroud, *Phys. Rev. B* **1997**, *56*, 8035.

[50] A. Lalisse, G. Tessier, J. Plain, G. Baffou, *J. Phys. Chem. C* **2015**, *119*, 25518.

[51] W. Hu, W. Zhen, M. Zhang, W. Wang, X. Jia, S. An, Y. Wang, Z. Guo, X. Jiang, *Adv. Healthcare Mater.* **2021**, *10*, 2101542.

[52] J. J. Rehr, J. J. Kas, F. D. Vila, M. P. Prange, K. Jorissen, *Phys. Chem. Chem. Phys.* **2010**, *12*, 5503.

© 2022 The Authors. Small published by Wiley-VCH GmbH

[53] Y. Pan, Y. Hang, X. Zhao, G. Liu, W. Jin, *J. Membr. Sci.* **2019**, *579*, 210.
[54] A. Alkhudhiri, N. Hilal, in *Emerging Technologies for Sustainable Desalination Handbook* (Ed: V. G. Gude), Butterworth-Heinemann, Oxford **2018**, p. 55.
[55] T. Horseman, Y. Yin, K. S. S. Christie, Z. Wang, T. Tong, S. Lin, *ACS ES&T Eng.* **2021**, *1*, 117.
[56] C. Zhang, H. Q. Liang, Z. K. Xu, Z. Wang, *Adv. Sci.* **2019**, *6*, 1900883.
[57] D. Winter, J. Koschikowski, M. Wieghaus, *J. Membr. Sci.* **2011**, *375*, 104.

© 2022 The Authors. Small published by Wiley-VCH GmbH